CARBON letters

Note

Carbon Letters Vol. 28, 105-110 (2018)

Catalytic effects of heteroatom-rich carbon-based freestanding paper with high active-surface area for vanadium redox flow batteries

Min Eui Lee, Hyo Won Kwak, and Hyoung-Joon Jin*

Department of Polymer Science and Engineering, Inha University, Incheon 22212, Korea

Article Info

Received 7 January 2018
Accepted 12 March 2018

***Corresponding Author**
E-mail: hjjin@inha.ac.kr
Tel: +82-32-860-7483

Open Access

DOI: http://dx.doi.org/10.5714/CL.2018.28.105

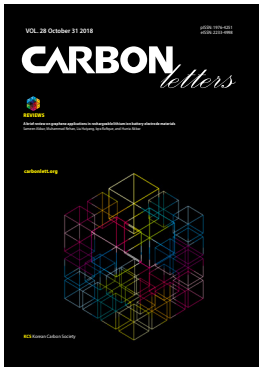

http://carbonlett.org

pISSN: 1976-4251
eISSN: 2233-4998

Abstract

Owing to their scalability, flexible operation, and long cycle life, vanadium redox flow batteries (VRFBs) have gained immense attention over the past few years. However, the VRFBs suffer from significant polarization, which decreases their cell efficiency. The activation polarization occurring during vanadium redox reactions greatly affects the overall performance of VRFBs. Therefore, it is imperative to develop electrodes with numerous catalytic sites and a long cycle life. In this study, we synthesized heteroatom-rich carbon-based freestanding papers (H-CFPs) by a facile dispersion and filtration process. The H-CFPs exhibited high specific surface area (~820 $m^2 g^{-1}$) along with a number of redox-active heteroatoms (such as oxygen and nitrogen) and showed high catalytic activity for vanadium redox reactions. The H-CFP electrodes showed excellent electrochemical performance. They showed low anodic and cathodic peak potential separation (ΔE_p) values of ~120 mV (positive electrolyte) and ~124 mV (negative electrolyte) in cyclic voltammetry conducted at a scan rate of 5 mV s^{-1}. Hence, the H-CFP-based VRFBs showed significantly reduced polarization.

Key words: catalytic effect, carbon-based freestanding papers, heteroatom, high active-surface area, vanadium redox flow batteries

1. Introduction

In response to increasing issues related to global climate change due to greenhouse gas emissions of carbon dioxide and nitrous oxide, renewable energy technologies have been developed to produce marketable energy from conversion of natural resources such as wind, solar, and tidal energy [1,2]. However, these renewable energies are difficult to use at a certain level owing to the influence of the changing environment. For this reason, next-generation electric energy storage (EES) including lithium-ion batteries, redox flow batteries (RFBs), fuel cells, and hydrogen storage is important to store the clean energy generated using renewable energy sources [4-7]. Among these, RFBs have gained immense attention. They are considered promising candidates for use in EES for large-scale applications due to their extensive scalability, design flexibility, and long cycle life [8-11]. In particular, vanadium redox flow batteries (VRFBs) possess efficiency advantages that derive from minimized ion crossover because the same vanadium salt is used as both positive and negative electrolyte. However, this results in loss of cell efficiency as well as increased cost of electrolyte [12-15]. Although the VRFBs have excellent merits, there is a fatal problem with its full-cell components that obstructs its practicality. The excessive cell polarization at high current densities is a major drawback of VRFBs and needs to be overcome to develop EES with high energy densities. Among the kinds of cell polarization, the activation polarization (originating from the electrodes) affects the electrode materials and their surface chemistry in ways that influence the vanadium redox reactions [16,17]. To reduce the activation polarization and achieve better cell performance, the morphology and surface chemistry

of the VRFB electrodes should be optimized by introducing an electro-catalyst such as oxygen or nitrogen functional groups [16-22]. Our recent results suggest that synergistic catalytic effects of the oxygen and nitrogen due to the pyridonic structure, leading to reduced activation polarization in the V^{2+}/V^{3+} redox reaction [21]. In addition, Wang et al. [22] reported that carbon felt dual-doped with nitrogen and oxygen and then used as electrodes exhibits superior battery performance (e.g., coulombic and voltage efficiencies) compared to pristine carbon felt. Consequently, this can be achieved by modifying the surface of the electrodes. Typically, carbon-based materials such as carbon or graphite felts are used as electrode materials for VRFBs, due to their high electric conductivity, high chemical stability in highly acidic environments, and relatively low cost [23,24]. Nevertheless, carbon-based electrodes are hydrophobic in nature and possess low active-surface areas; hence, they exhibit poor electrochemical activity. To overcome these issues, many recent efforts have been made to develop electrodes with high active-surface area and superior catalytic activity towards vanadium redox reactions [23-25]. In contrast, nanocarbon-based materials such as carbon nanofibers, carbon nanotubes, and graphene show excellent catalytic activity towards vanadium redox reactions because of its inherently superior high-active surface area and electrical conductivity [26-28]. In addition, biomass-derived nanocarbon electrodes also exhibit high electrochemical activity owing to their high active-surface area and to the natural presence of numerous heteroatoms on their surface [29-32]. Although nanocarbon materials show outstanding electrochemical properties, most of them, including such as carbon felts or carbon papers, must be used on substrates if they are to be used as VRFB electrodes. Recently, freestanding carbon sheets obtained from multiwall carbon nanotubes have been reported to be electrochemically active towards the VO^{2+}/VO_2^+ and V^{2+}/V^{3+} redox couples, and hence have become potential candidates for VRFB electrodes [33]. To develop a plausible nanocarbon-based active electrode, it is essential to realize a monolithic form showing high electrocatalytic activity for vanadium redox couples. In this study, heteroatom-rich carbon-based freestanding papers (H-CFPs) were prepared using materials of acid-treated carbon nanotubes (A-CNTs) and microporous carbon-based nanoplates containing numerous heteroatoms (H-CMNs). These were collected by simple filtration into a monolithic form. The prepared H-CFPs were freestanding (did not require any binder) and contained numerous electroactive heteroatoms, leading to a catalytic effect for vanadium redox reactions. The H-CFPs also showed high active-surface area, numerous heteroatoms, and great acid stability. These all support superior electrochemical activity, and make H-CFPs potential candidates for use as VRFB electrodes.

2. Experimental

2.1. Preparation of H-CFPs

The H-CFPs were prepared from A-CNTs and H-CMNs using a facile dispersion and filtration process. The detailed procedure for the synthesis of these samples has been reported elsewhere [34,35]. To prepare the H-CFPs, we first prepared two dispersions. The first was of 1:1 (by weight) A-CNTs in dimethylformamide (DMF) solution and the second was of H-CMNs in DMF (same ratio). The two dispersions were then stirred for 30 min and vacuum filtered onto an alumina template membrane to obtain freestanding films. The resulting products were then washed with ethanol and water to obtain the H-CFPs and dried in a vacuum oven at 80°C for 3 h. Finally, the alumina membrane was peeled off. For comparison with the H-CFPs, freestanding films containing only A-CNTs were also prepared through the same process, excluding the addition of H-CMNs.

2.2. Characterization

The morphology of the H-CFPs was observed using field-emission scanning electron microscopy (FE-SEM; S-4300SE, Hitachi). X-ray diffraction (XRD) analysis of the H-CFPs and A-CNTs was performed using an X-ray diffractometer (DMAX-2500, Rigaku). Raman spectra of the samples were acquired using a Raman microscope with a polarized laser (514.5 nm). The acquisition time and number of scans to obtain each spectrum were 15 s and five cycles, respectively. The Brunauer-Emmett-Teller (BET) surface area was determined using nitrogen adsorption and a desorption analyzer (ASAP 2020, Micromeritics) at −196°C. The surface chemistry of the samples was determined using X-ray photoelectron spectroscopy (XPS; PHI 5700 ESCA).

2.3. Electrochemical characterization

Cyclic voltammetry (CV) and electrochemical impedance spectroscopy (EIS) analyses were carried out using a potentiostat (PGSTAT302N, Autolab) and a home-made cell with three electrodes (working, counter, and reference) [36]. H-CFP and A-CNT electrodes with a diameter of 5 mm (area=0.196 cm^2) were employed as working electrodes. Pristine carbon felt with an area of 3 cm^2 and Ag/AgCl, were used as the counter and reference electrodes, respectively. The positive (0.1 M $VOSO_4$ / 2.0 M H_2SO_4) and negative (0.1 M $V_2(SO_4)_3$ / 2.0 M H_2SO_4) electrolytes for the half-cell tests were prepared using $VOSO_4$ (99.5%, Sigma-Aldrich) and H_2SO_4 (96.5%, Sigma-Aldrich).

3. Results and Discussion

The morphology of a prepared electrode can be observed in Fig. 1a and b, which shows the optical and FE-SEM images of the H-CFPs. The H-CMNs had a graphene-like two-dimensional structure that induced brittleness in them. On the other hand, the H-CFPs were suitable, freestanding, and formed a pliable electrode because of the presence of the A-CNTs. In detail, the scheme in Fig. 1c represents a concise procedure for the fabrication of the H-CFPs. To confirm the carbon structures and texture properties of both the A-CNT and H-CFP samples, XRD, Raman, and porosimetry analyses were carried out. The XRD pattern of the H-CFPs showed a relatively broad graphite (002) peak at ~25.5° while a sharp peak was observed in the case of the A-CNTs (Fig. 2a). The (002) peak derives from the stacking order of the graphene layers. Because the H-CMNs were

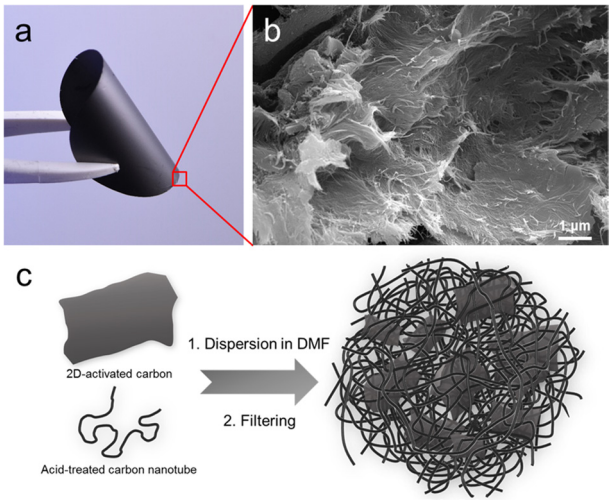

Fig. 1. (a) Optical image of the H-CFPs, (b) FE-SEM image of the H-CFPs, and (c) schematic for the preparation of the H-CFPs.

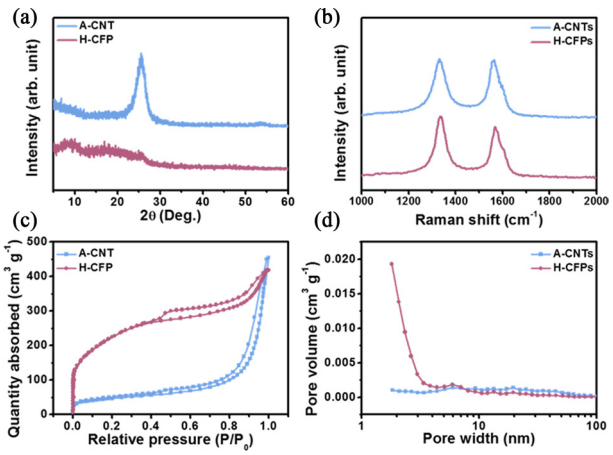

Fig. 2. (a) XRD pattern, (b) Raman spectra, (c) nitrogen adsorption-desorption isotherms, and (d) pore size distribution of the A-CNTs and H-CFPs.

prepared by chemical activation using alkali agents, insufficient carbon-layer stacking was observed due to exfoliation of the graphite structure. This resulted in disordering of the carbon structure [35]. The Raman spectra of the A-CNTs and H-CFPs showed distinct *D* and *G* bands at 1331 and 1336 cm^{-1} (for A-CNTs) and 1563 and 1568 cm^{-1} (for H-CFPs) (Fig. 2b). The *D* bands correspond to the intrinsic phonon modes with the A_{1g} symmetry of aromatic rings (which are activated by structural disorder), while the *G* bands correspond to the hexagonal carbon structure related to the E_{2g} vibration mode of the sp^2-hybridized C atoms [37]. The *D*/*G* intensity ratio (I_D/I_G) of the H-CFPs was ~1.22, which is much higher than that of the A-CNTs (~1.01). This result indicates that the H-CFPs formed a disordered carbon structure containing numerous defects (such as heteroatoms), which is in good agreement with the XRD results. The pore structure of the A-CNTs and H-CFPs was examined using their nitrogen adsorption and desorption isotherms (Fig. 2c). The pore size distribution of the A-CNTs and H-CFPs is shown in

Table 1. Textural properties of the A-CNTs and H-CFPs

Sample	S_{BET} ($m^2 g^{-1}$)[a)]	$^bS_{MIC}$ ($m^2 g^{-1}$)[b)]	$^cS_{MESO}$ ($m^2 g^{-1}$)[c)]
H-CFPs	820.9	82.2	738.8
A-CNTs	166.1	43.0	123.1

[a)] S_{BET}: BET specific surface area.
[b)] S_{MIC}: micropore specific surface area.
[c)] S_{MESO}: mesopore specific surface area.

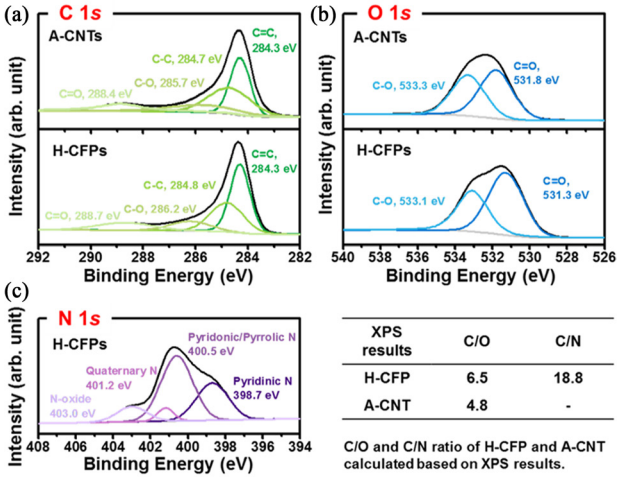

XPS results	C/O	C/N
H-CFP	6.5	18.8
A-CNT	4.8	-

C/O and C/N ratio of H-CFP and A-CNT calculated based on XPS results.

Fig. 3. (a) C 1*s* and (b) O 1*s* XPS spectra of the A-CNTs and H-CFPs, and (c) N 1*s* XPS spectrum of the H-CFPs.

Fig. 2d. It can be seen that the A-CNTs and H-CFPs show a low relative pressure region (~0.02), indicating some increase in the adsorbed nitrogen (~43 and ~150 $cm^3 g^{-1}$) (Fig. 2c). These results indicate that the adsorption of nitrogen molecules at low relative pressure is induced by the deposition of a monolayer on the surface of both A-CNTs and H-CFPs [34,35]. The H-CFPs showed a higher specific surface area (~820.9 $m^2 g^{-1}$) than for the A-CNTs (~166.1 $m^2 g^{-1}$). In addition, the H-CFPs exhibited type-I and type-IV isotherms, indicating their microporous and mesoporous structure, respectively. The porous structure and high surface area of the H-CFPs provided a large number of active sites for vanadium redox reactions, which improved their catalytic activity [29-32]. The textural properties of the A-CNTs and H-CFPs obtained from nitrogen adsorption and desorption isotherms are given in Table 1. XPS analysis was also conducted to elucidate the surface chemistry of A-CNTs and H-CFPs, and their related carbon nanostructure. The results showed the presence of heteroatoms in the A-CNT and H-CFP samples (Fig. 3). The high-resolution C 1*s* spectra of both the A-CNTs and H-CFPs indicated the presence of various bonds such as C=C, C-C, C-O, and C=O and they also showed relatively similar C/O ratios. Moreover, the XPS spectra of the H-CFPs indicated the presence of nitrogen functional groups, in that the peaks for pyridinic-N, pyridonic/pyrrole-N, quaternary-N, and N-O bonds were observed at 398.7, 400.5, 401.2, and 403.0 eV, respectively. The value of a C/N ratio of ~4.8 was obtained, in-

Table 2. Electrochemical properties obtained from the cyclic voltammetry results of the A-CNT and H-CFP electrodes at various scan rates

Scan rate (mV s^{-1})	A-CNTs				H-CFPs			
	Negative electrolyte		Positive electrolyte		Negative electrolyte		Positive electrolyte	
	I_{pa}/I_{pc}	DE_p (mV)	I_{pa}/I_{pc}	DE_p (mV)	I_{pa}/I_{pc}	DE_p (mV)	I_{pa}/I_{pc}	DE_p (mV)
1	0.53	70.5	1.21	90.6	0.58	57.3	1.07	60.4
2	0.65	96.4	1.11	130.9	0.71	79.9	1.09	82.9
3	0.72	120.9	1.12	161.1	0.76	94.6	1.08	90.6
5	0.77	154.9	1.12	221.5	0.81	124.8	1.07	120.9
7	0.74	186.1	1.11	272.3	0.83	141.0	1.08	151.0
10	0.74	227.9	1.13	322.4	0.85	174.1	1.10	161.1

dicating the presence of abundant nitrogen as well as oxygen at the active sites of the vanadium ion (Fig. 3c) [16-22]. The electrochemical performance of the A-CNT and H-CFP samples was investigated by carrying out CV measurements using a home-made three-electrode cell system at room temperature [21,32,36]. In the presence of the positive electrolyte, the A-CNT and H-CFP samples showed peak potential separation (ΔE_p) of ~221 and ~120 mV, respectively. On the other hand, in the presence of the negative electrolyte, the A-CNT and H-CFP samples showed ΔE_p of ~154 and ~124 mV, respectively (Fig. 4a and b). In the presence of the positive electrolyte, the I_{pa}/I_{pc} ratio (for the VO^{2+}/VO_2^+ redox reaction at a scan rate of 5 mV s^{-1}) for the H-CFP electrodes was close to one (~1.07) while the A-CNT electrodes showed a I_{pa}/I_{pc} ratio of ~1.12. As shown in Fig. 4c and d, the peak current densities of the as-prepared electrodes were almost proportional to the square root of the scan rate. This suggests that a mass transfer process resulted in the occurrence of the VO^{2+}/VO_2^+ and V^{2+}/V^{3+} redox reactions on the surface of the electrodes. Compared to the slope of the H-CFP and the A-CNT, the H-CFP electrodes showed a much higher slope than for the A-CNT electrodes. The higher slope of the H-CFP electrode means that a faster rate of mass transfer occurs to the H-CFP surface [26]. This fast mass transfer of H-CFP could be attributed to the high active-surface area and to the numerous oxygen and nitrogen functional groups on the H-CFP surface. The results discussed so far show that the electrochemical catalytic effects of the H-CFP electrodes reduced their activation polarization. The electrochemical properties of these electrodes are given in Table 2. To examine the polarization resistance of the as-prepared electrodes, EIS was carried out under equivalent conditions and the Nyquist plots are shown in Fig. 4e and f. The radius of the semicircular part of the Nyquist plots was affected by the activation polarization (for the vanadium redox reactions) of the electrodes [21,33]. In the high-frequency region of the semicircular part, the H-CFP electrodes showed a lower charge transfer resistance for the VO^{2+}/VO_2^+ redox reaction than with the A-CNT electrodes. However, in the presence of the negative electrolyte, the charge transfer resistance of both electrodes was almost the same (see Fig. 4d). These results demonstrate the potential of H-CFPs: facile ion and electron transport and superior catalytic activity, leading to reduced activation polarization of the VRFB electrodes.

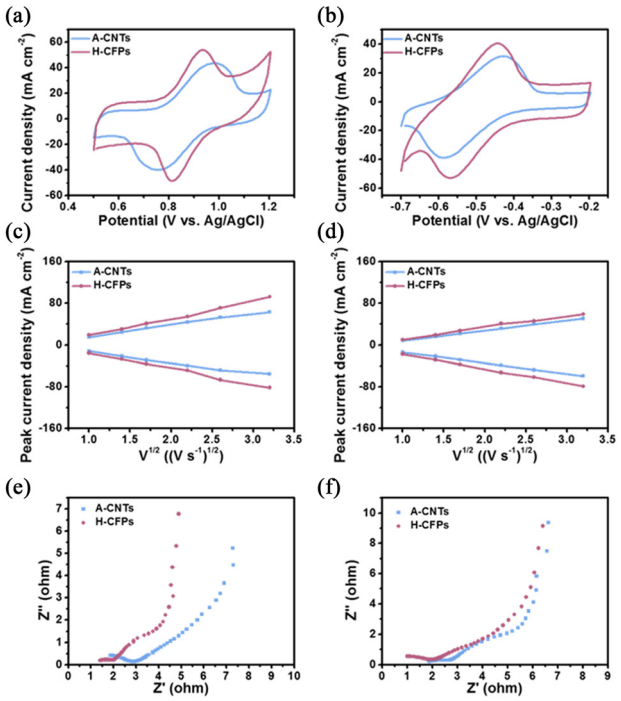

Fig. 4. Cyclic voltammograms of the A-CNT and H-CFP electrodes (a) VO^{2+}/VO_2^+ and V^{2+}/V^{3+} redox couple in a 0.1 M $VOSO_4$ + 2 M H_2SO_4 electrolyte at a scan rate of 5 mV s^{-1}. Peak current densities of the A-CNT and H-CFP electrodes in the (c) catholyte and (d) anolyte. Nyquist plots of the A-CNT and H-CFP electrodes in the (e) catholyte and (f) anolyte.

4. Conclusions

In summary, H-CFPs were prepared using a facile dispersion and filtration process. The H-CFPs possessed an entangled structure (1- and 2-D) for mass transport. In addition, the H-CFPs showed the presence of numerous heteroatoms (such as oxygen and nitrogen atoms) that acted as active sites for the vanadium ions, and a high specific surface area of ~820 m^2 g^{-1}. These characteristics are attributed to their superior electrochemical performance, leading to superior catalytic activity with ΔE_p values of ~120 mV (positive electrolyte) and ~124 mV (nega-

tive electrolyte) (as revealed by their CV test conducted at 5 mV s^{-1}). These results show that H-CFPs are a candidate material for VRFB electrodes.

Conflict of Interest

No potential conflict of interest relevant to this article was reported.

Acknowledgements

This work was financially supported by an Inha University Research Grant.

References

[1] Chu S, Majumdar A. Opportunities and challenges for a sustainable energy future. Nature, **488**, 294 (2012). https://doi.org/10.1038/nature11475.

[2] Dunn B, Kamath H, Tarascon JM. Electrical energy storage for the grid: a battery of choices. Science, **334**, 928 (2011). https://doi.org/10.1126/science.1212741.

[3] Tarascon JM, Armand M. Issues and challenges facing rechargeable lithium batteries. Nature, **414**, 359 (2001). https://doi.org/10.1038/35104644.

[4] Larcher D, Tarascon JM. Towards greener and more sustainable batteries for electrical energy storage. Nat Chem, **7**, 19 (2015). https://doi.org/10.1038/nchem.2085.

[5] Muñoz PM, Correa G, Gaudiano ME, Fernández D. Energy management control design for fuel cell hybrid electric vehicles using neural networks. Int J Hydrogen Energy, **42**, 28932 (2017). https://doi.org/10.1016/j.ijhydene.2017.09.169.

[6] Sangsefidi FS, Salavati-Niasari M, Varshoy S, Shabani-Nooshabadi M. Investigation of Mn_2O_3 as impurity on the electrochemical hydrogen storage performance of MnO_2-CeO_2 nanocomposites. Int J Hydrogen Energy, **42**, 28473 (2017). https://doi.org/10.1016/j.ijhydene.2017.09.144.

[7] Mayer T, Kreyenberg D, Wind J, Braun F. Feasibility study of 2020 target costs for PEM fuel cells and lithium-ion batteries: a two-factor experience curve approach. Int J Hydrogen Energy, **37**, 14463 (2012). https://doi.org/10.1016/j.ijhydene.2012.07.022.

[8] Wang W, Luo Q, Li B, Wei X, Li L, Yang Z. Recent progress in redox flow battery research and development. Adv Funct Mater, **23**, 970 (2013). https://doi.org/10.1002/adfm.201200694.

[9] Lin K, Chen Q, Gerhardt MR, Tong L, Kim SB, Eisenach L, Valle AW, Hardee D, Gordon RG, et al. Alkaline quinone flow battery. Science, **349**, 1529 (2015). https://doi.org/10.1126/science.aab3033.

[10] Park M, Ryu J, Wang W, Cho J. Material design and engineering of next-generation flow-battery technologies. Nat Rev Mater, **2**, 16080 (2016). https://doi.org/10.1038/natrevmats.2016.80.

[11] Li L, Kim S, Wang W, Vijayakumar M, Nie Z, Chen B, Zhang J, Xia G, Hu J, Graff G, et al. A stable vanadium redox-flow battery with high energy density for large-scale energy storage. Adv Energy Mater, **1**, 394 (2011). https://doi.org/10.1002/aenm.201100008.

[12] Skyllas-Kazacos M, Rychcik M, Robins RG, Fane AG, Green MA. New all-vanadium redox flow cell. J Electrochem Soc, **133**, 1057 (1986). https://doi.org/10.1149/1.2108706.

[13] Skyllas-Kazacos M, Grossmith F. Efficient vanadium redox flow cell. J Electrochem Soc, **134**, 2950 (1987). https://doi.org/10.1149/1.2100321.

[14] Su L, Zhang D, Peng S, Wu X, Luo Y, He G. Orientated graphene oxide/Nafion ultra-thin layer coated composite membranes for vanadium redox flow battery. Int J Hydrogen Energy, **42**, 21806 (2017). https://doi.org/10.1016/j.ijhydene.2017.07.049.

[15] Sadhasivam T, Kim HT, Park WS, Lim H, Ryi SK, Roh SH, Jung HY. Low permeable composite membrane based on sulfonated poly(phenylene oxide) (sPPO) and silica for vanadium redox flow battery. Int J Hydrogen Energy, **42**, 19035 (2017). https://doi.org/10.1016/j.ijhydene.2017.06.030.

[16] Park M, Jeon IY, Ryu J, Baek JB, Cho J. Exploration of the effective location of surface oxygen defects in graphene-based electrocatalysts for all-vanadium redox-flow batteries. Adv Energy Mater, **5**, 1401550 (2014). https://doi.org/10.1002/aenm.201401550.

[17] Park M, Ryu J, Kim Y, Cho J. Corn protein-derived nitrogen-doped carbon materials with oxygen-rich functional groups: a highly efficient electrocatalyst for all-vanadium redox flow batteries. Energy Environ Sci, **7**, 3727 (2014). https://doi.org/10.1039/c4ee02123a.

[18] Pezeshki AM, Clement JT, Veith GM, Zawodzinski TA, Mench MM. High performance electrodes in vanadium redox flow batteries through oxygen-enriched thermal activation. J Power Sources, **294**, 333 (2015). https://doi.org/10.1016/j.jpowsour.2015.05.118.

[19] Kim J, Lim H, Jyoung JY, Lee ES, Yi JS, Lee D. High electrocatalytic performance of N and O atomic co-functionalized carbon electrodes for vanadium redox flow battery. Carbon, **111**, 592 (2017). https://doi.org/10.1016/j.carbon.2016.10.043.

[20] Kim KJ, Lee HS, Kim J, Park MS, Kim JH, Kim YJ, Skyllas-Kazacos M. Superior electrocatalytic activity of a robust carbon-felt electrode with oxygen-rich phosphate groups for all-vanadium redox flow batteries. ChemSusChem, **9**, 1329 (2016). https://doi.org/10.1002/cssc.201600106.

[21] Lee ME, Jin HJ, Yun YS. Synergistic catalytic effects of oxygen and nitrogen functional groups on active carbon electrodes for all-vanadium redox flow batteries. RSC Adv, **7**, 43227 (2017). https://doi.org/10.1039/c7ra08334c.

[22] Huang Y, Deng Q, Wu X, Wang S. N, O Co-doped carbon felt for high-performance all-vanadium redox flow battery. Int J Hydrogen Energy, **42**, 7177 (2017). https://doi.org/10.1016/j.ijhydene.2016.04.004.

[23] Dixon D, Babu DJ, Langner J, Bruns M, Pfaffmann L, Bhaskar A, Schneider JJ, Scheiba F, Ehrenberg H. Effect of oxygen plasma treatment on the electrochemical performance of the rayon and polyacrylonitrile based carbon felt for the vanadium redox flow battery application. J Power Sources, **332**, 240 (2016). https://doi.org/10.1016/j.jpowsour.2016.09.070.

[24] Liu T, Li X, Nie H, Xu C, Zhang H. Investigation on the effect of catalyst on the electrochemical performance of carbon felt and graphite felt for vanadium flow batteries. J Power Sources, **286**, 73 (2015). https://doi.org/10.1016/j.jpowsour.2015.03.148.

[25] Kabtamu DM, Chen JY, Chang YC, Wang CH. Water-activated graphite felt as a high-performance electrode for vanadium redox flow batteries. J Power Sources, **341**, 270 (2017). https://doi.org/10.1016/j.jpowsour.2016.12.004.

[26] Park M, Jung Y, Kim J, Lee HI, Cho J. Synergistic effect of carbon nanofiber/nanotube composite catalyst on carbon felt electrode for

high-performance all-vanadium redox flow battery. Nano Lett, **13**, 4833 (2013). https://doi.org/10.1021/nl402566s.

[27] Li W, Liu J, Yan C. Multi-walled carbon nanotubes used as an electrode reaction catalyst for VO_2^+/VO^{2+} for a vanadium redox flow battery. Carbon, **49**, 3463 (2011). https://doi.org/10.1016/j.carbon.2011.04.045.

[28] Han P, Wang H, Liu Z, Chen X, Ma W, Yao J, Zhu Y, Cui G. Graphene oxide nanoplatelets as excellent electrochemical active materials for VO_2^+/VO^{2+} and V^{2+}/V^{3+} redox couples for a vanadium redox flow battery. Carbon, **49**, 693 (2011). https://doi.org/10.1016/j.carbon.2010.10.022.

[29] Zhang ZH, Zhao TS, Bai BF, Zeng L, Wei L. A highly active biomass-derived electrode for all vanadium redox flow batteries. Electrochim Acta, **248**, 197 (2017). https://doi.org/10.1016/j.electacta.2017.07.129.

[30] Maharjan M, Bhattarai A, Ulaganathan M, Wai N, Oo MO, Wang JY, Lim TM. High surface area bio-waste based carbon as a superior electrode for vanadium redox flow battery. J Power Sources, **362**, 50 (2017). https://doi.org/10.1016/j.jpowsour.2017.07.020.

[31] Ulaganathan M, Jain A, Aravindan V, Jayaraman S, Ling WC, Lim TM, Srinivasan MP, Yan Q, Madhavi S. Bio-mass derived mesoporous carbon as superior electrode in all vanadium redox flow battery with multicouple reactions. J Power Sources, **274**, 846 (2015). https://doi.org/10.1016/j.jpowsour.2014.10.176.

[32] Lee ME, Lee S, Jin HJ, Yun YS. Standalone macroporous graphitic nanowebs for vanadium redox flow batteries. J Ind Eng Chem, **60**, 85 (2018). https://doi.org/10.1016/j.jiec.2017.09.043.

[33] Mustafa I, Lopez I, Younes H, Susantyoko RA, Al-Rub RA, Almheiri S. Fabrication of freestanding sheets of multiwalled carbon nanotubes (Buckypapers) for vanadium redox flow batteries and effects of fabrication variables on electrochemical performance. Electrochim Acta, **230**, 222 (2017). https://doi.org/10.1016/j.electacta.2017.01.186.

[34] Yun YS, Lee ME, Joo MJ, Jin HJ. High-performance supercapacitors based on freestanding carbon-based composite paper electrodes. J Power Sources, **246**, 540 (2014). https://doi.org/10.1016/j.jpowsour.2013.08.011.

[35] Yun YS, Park KY, Lee B, Cho SY, Park YU, Hong SJ, Kim BH, Gwon H, Kim H, Lee S, et al. Sodium-ion storage in pyroprotein-based carbon nanoplates. Adv Mater, **27**, 6914 (2015). https://doi.org/10.1002/adma.201502303.

[36] Park JH, Park JJ, Park OO, Jin CS, Yang JH. Highly accurate apparatus for electrochemical characterization of the felt electrodes used in redox flow batteries. J Power Sources, **310**, 137 (2016). https://doi.org/10.1016/j.jpowsour.2016.02.005.

[37] Kudin KN, Ozbas B, Schniepp HC, Prud'homme RK, Aksay IA, Car R. Raman spectra of graphite oxide and functionalized graphene sheets. Nano Lett, **8**, 36 (2008). https://doi.org/10.1021/nl071822y.

[38] Yoon HJ, Lee ME, Kim, NR, Yang SJ, Jin HJ, Yun YS. Hierarchically nanoporous pyropolymer nanofibers for surface-induced sodium-ion storage. Electrochim Acta, **242**, 38 (2017). https://doi.org/10.1016/j.electacta.2017.05.014.